Journal of Materials Chemistry A

Accepted Manuscript

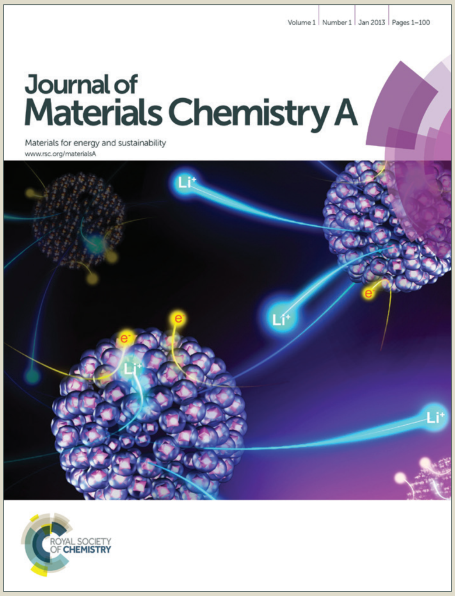

ROYAL SOCIETY OF CHEMISTRY

www.rsc.org/materialsA

Nanostructured cobalt sulfide-on-fiber with tunable morphology as electrodes for asymmetric hybrid supercapacitors

R.B. Rakhi, Nuha Alhebshi, D.H. Anjum and H.N. Alshareef*

Material Science and Engineering, King Abdullah University of Science and Technology
(KAUST), Thuwal 23955-6900, Saudi Arabia

*Corresponding author: husam.alshareef@kaust.edu.sa

Phone: Office: +966-(0)2-808-4477 | Cell: +966-(0)5-44700037

ABSRACT

Porous cobalt sulfide (Co_9S_8) nanostructures with tunable morphology, but identical crystal phase and composition, have been directly nucleated over carbon fiber and evaluated as electrodes for asymmetric hybrid supercapacitors. As the morphology is changed from two-dimensional (2D) nanoflakes to 3D octahedra, dramatic changes in supercapacitor performance are observed. In three-electrode configuration, the binder-free Co_9S_8 2D nanoflake electrodes show a high specific capacitance of 1056 F/g at 5 mV/s vs 88F/g for the 3D electrodes. As sulfides are known to have low operating potential, for the first time, asymmetric hybrid supercapacitors are constructed from Co_9S_8 nanostructures and activated carbon (AC), providing an operation potential from 0 to 1.6V. At a constant current density of 1 A/g, the 2D Co_9S_8 , nanoflake //AC asymmetric hybrid supercapacitor exhibits a gravimetric cell capacitance of 82.9 F/g, which is much higher than that of AC//AC symmetric capacitor (44.8 F/g). Moreover, the asymmetric hybrid supercapacitor shows an excellent energy density of 31.4 Wh/kg at a power density of 200 W/Kg and an excellent cycling stability with capacitance retention of ~90 % after 5000 cycles.

KEYWORDS

Co_9S_8 nanoflakes, Co_9S_8 octahedra, asymmetric hybrid supercapacitor, gravimetric cell capacitance, cycling stability

INTRODUCTION

Symmetric double-layer supercapacitor are promising devices for hybrid electric vehicle applications due to their long term cycling stability, high power density, and excellent charge/discharge characteristics [1-3]. However, the lower energy density of symmetric supercapacitors as compared to rechargeable battery systems, limits their industrial utilization for energy storage[3]. Therefore, much of the research activity on supercapacitors is concentrated on improving the energy density of these devices by a variety of approaches [4].

An asymmetric hybrid supercapacitor - consisting of a negative electrode based on an electric double layer capacitive (EDLC) material and a positive electrode based on a pure pseudocapacitive material, with a larger working voltage leading to a notable improvement in the energy density - can be considered as a promising alternative to symmetric double-layer supercapacitor [5-9]. Carbon-based materials such as graphene, activated carbon, carbon nanotubes, carbon nanofibers, and mesoporous carbon, are commonly used as electrode materials in the negative electrode, in which the charge storage mechanism is mostly based on electric double-layer (non-Faradic or electrostatic) absorption/desportion [10]. Among the different types of carbon materials, activated carbon(AC) is the most popular negative electrode material for hybrid capacitors because of its high surface area and relatively good electrical conductivity[6, 11]. Conducting polymers, transition metal oxides, lithium intercalation compounds, etc. are the generally used electrode materials in the pseudocapacitive electrode, where the charge storage mechanism is mainly based on redox (Faradic) reactions with or without non-faradic reactions[10].

In the last few years, nanostructured transition-metal chalcogenides have attracted substantial research attention, as a new class of electrode materials for pseudocapacitors [12, 13].

Studies reveal that metal sulfides can also undergo redox transitions among different valence states of metal ions, in a similar way as in metal oxides [14, 15]. Many reports are available on the supercapacitive properties of different types of metal sulfides such as zinc sulphide[16], copper sulfide[17], molybdenum disulfide[18], nickel sulfide[19], cobalt sulfide[14], nickel cobalt sulfide[13], and so on. Among these different types of metal sulfides, cobalt sulfide (general formula Co_xS_y) is reported to be the most promising pseudocapacitive material in alkaline electrolyte, with its high capacitance, good rate capability, and excellent cycling stability[17]. As the electrochemical performance of pseudocapacitive materials largely depends on their morphology and surface area, the development of controlled synthesis techniques of cobalt sulfide nanostructures with high surface area is vitally important. Many reports are available on the synthesis and supercapacitor properties of CoS nanostructures with different morphologies [12, 15, 20, 21]. In 2008, Bao *et al.* reported biomolecule-assisted hydrothermal process to synthesize cobalt sulfide (CoS) nanowires which exhibited a specific capacitance of 508 F/g at a constant current density of 2.5 mA/cm[221]. In 2010, P.Justin and G. Ranga Rao reported the controlled synthesis of CoS nanospheres with a specific capacitance of 363 F/ g at a scan rate of 5 mV/s [15]. Jeng-Yu Lin and Shu-Wei Chou reported the preparation and supercapacitive performance of an interlaced nanosheet-like cobalt sulfide (CoS) electroactive material over Ni foam substrate[22]. An impressive specific capacitance, as high as 1471 F /g at a constant current density of 4 A/g, was achieved for the interlaced nanosheet-like CoS electroactive material[22]. Wan *et al.* reported hydrothermal synthesis of CoS nanotubes which exhibited a specific capacitance of of 285 F/g at the current density of 0.5 A/g[12]. All these measurements were carried out in 3 electrode configuration in aqueous KOH electrolyte.

Sulfuration of cobalt based precursor is an efficient way to prepare other forms of cobalt sulfide with controlled nanostructures like Co_3S_4 and Co_9S_8. In 2013, Chen *et al.* reported the shape and phase transformation synthesis of Ni foam supported Co_3S_4 nanosheet arrays with a remarkable high specific capacitance of 1081 F/g at 1.61 A/g in 3 electrode configuration [23]. In a recent work, Pu *et al.* reported nickel-supported Co_9S_8 nanotube arrays by the sulfuration of $Co(CO_3)0.35Cl_{0.20}(OH)_{1.10}$ nanoneedles. The Co_9S_8 nanotube arrays electrode exhibited a high specific capacitance of 1775 F/g at 4 A/g, in 3 electrode configuration [20]. But, in 2011, Xing *et al.* successfully demonstrated that the use of nickel foam as current collector can bring about substantial errors to the specific capacitance values of electrode materials [24]. In 2013, Xu *et al.* reported the fabrication of flexible asymmetric inorganic-inorganic supercapacitors based on acicular Co_9S_8 nanorod arrays –prepared by the sulfuration technique on woven carbon fabrics - as positive electrode and $Co_3O_4@RuO_2$ nanosheet arrays as negative electrode. In this case both the electrodes were made of pseudocapacitive materials [25]. To the best of our knowledge, no reports are available on the fabrication of asymmetric hybrid supercapacitors with cobalt sulfides (Co_9S_8/Co_3S_4) as positive electrodes.

In this paper, for the first time, we repot the fabrication and performance studies of two aqueous asymmetric hybrid supercapacitors, each consisting of Co_9S_8 with a particular morphology (nanoflakes or octahedra) as the positive electrode and AC as the negative electrode. By fixing the chemical phase and composition of Co_9S_8, we could better investigate the effect of morphology, particularly 2D morphology, on the electrochemical activity and performance of the Co_9S_8 electrodes. A 30 wt% aqueous KOH has been used as the electrolyte.

EXPERIMENTAL

Synthesis of cobalt sulfide nanostructures over carbon fiber cloth was performed using a two-step hydrothermal route. In the first step, Co_3O_4 nanostructures with different morphologies were directly grown over carbon cloth and in the second, these nanostructures were converted to Co_9S_8 retaining their original nanostructure by a hydrothermal sulfuration process.

Direct Growth of Co_3O_4 Nanostructures over Carbon Fiber. Two dimensional (2 D) Co_3O_4, nanoflakes were directly grown over carbon fiber cloth by a simple hydrothermal method. 1.5g $Co(NO_3)_2{\cdot}6H_2O$, 10 mg Hexa decyl trimethyl ammonium Bromide (CTAB) and 10 ml of Ethylene glycol were dissolved in 50 ml DI water by vigorous magnetic stirring. Resulting solution was divided into two halves and each portion was then transferred into a 40 ml Teflon-lined stainless steel autoclave. A piece of carbon fiber cloth (1cm × 2 cm),was immersed in the growth solution in the autoclave followed by heating the autoclave in an oven at 160 ºC for 20 h to allow growth of Co_3O_4 nanoflakes. In order to achieve the octahedral morphology of Co_3O_4, a simple solvothermal method was used. 2 g $Co(NO_3)_2{\cdot}6H_2O$, 1g Hexa decyl trimethyl ammonium Bromide (CTAB) and 6 ml water were dissolved in 30 ml absolute methanol by vigorous magnetic stirring. Resulting solution was then transferred into a 40 ml Teflon- lined stainless steel autoclave. A piece of carbon fiber cloth (1cm × 2 cm),was immersed in the growth solution in the autoclave followed by heating the autoclave in an oven at 160 ºC for 20 h to allow growth of Co_3O_4 octahedra. In both the cases, the substrates covered with final products were washed with H_2O and ethanol, dried in a vacuum at 120 ºC for 10h, and then calcined at 250 ºC for 4h. In both these cases, Mechanism of formation probably proceeds through the following reactions.

$Co(NO_3)_2$ exists as Co^{2+} and $NO3^-$ ions in the solution

$$Co(NO_3)_2 \rightarrow Co^{2+} + NO_3^- \qquad (1)$$

The cobalt ions (Co^{2+}) from the $Co(NO_3)_2$ solution react with hydroxyl ions forming α cobalt hydroxide. The α form is unstable and rapidly changes to β cobalt hydroxide.

$$Co^{2+} + 2OH^{-} \rightarrow (\alpha) - Co(OH)_2 \rightarrow (\beta) - Co(OH)_2 \qquad (2)$$

The hydroxide converts to stable oxide phase upon reaction with oxygen.

$$Co(OH)_2 + O_2 \rightarrow Co_3O_4 + H_2O \qquad (3)$$

In the presence of Ethylene glycol the Co_3O_4 nanoparticles aggregates together to form nanoflakes of nanosheets. In the presence of CTAB and methanol, the reaction rate increases and the nanoflakes combine together to form octahedra.

Synthesis of Co_9S_8 Nanostructures over Carbon Fiber. Co_3O_4 nanostructures grown over carbon cloth (1cm × 2 cm) were soaked in a 25 mL solution containing 1 g of Na_2S in a 40 ml Teflon- lined stainless steel autoclave. After being sealed, the autoclave was heated at 120 ºC for 24 h. The final products were washed with distilled water several times and dried at 50 ºC under vacuum. The weight of final deposit was accurately calculated using an analytical micro balance. (XP 26 Mettler Toledo, max 22g, 0.001mg of resolution).

Preparation of Negative Electrode. AC was mixed with polytetrafluoroethylene (PTFE) binder in a mass ratio of 95:5 and dispersed in ethanol. The resulting mixture was homogenized by ultrasonication and coated onto the carbon cloth (Fuel cell stores) substrate, which was followed by drying at 100 ºC for 12 h in a vacuum oven.

General Characterization. Crystal structure of Cobalt sulfide nanostructures were analysed by a powder X-ray diffraction system (XRD, Bruker, D8 ADVANCE) equipped with Cu K_α radiation (λ= 0.15406 nm). Brunauer–Emmett–Teller (BET) surface area of the samples were determined using surface area and porosimetry system 'Micromeritics' (ASAP 2420) at 77 K. Before measurements, the samples were dried at 70 ˚C for 10 h in a Vacuum oven and then degassed at 200 ˚C for 12 h until the vacuum was less than 2 µm Hg. The surface morphology and microstructure of the samples were investigated by a scanning electron microscopy (SEM, FEI Helios NanoLab) and transmission electron microscopy (TEM, FEI Titan).

Electrochemical Characterization. To construct an asymmetric hybrid supercapacitor, the loading mass ratio of active materials (Co_9S_8 /AC) was estimated from their individual specific capacitances measured in three-electrode configuration, in which a platinum foil and a Ag/AgCl were used as counter electrode and reference electrode, respectively. The supercapacitive performances of the AC based symmetric supercapacitor and that of asymmetric hybrid supercapacitor consisting of Co_9S_8 nanostructure as the positive electrode and AC as negative electrode separated by a monolayer polypropylene separator (25µm thick, Celgard 3501) were performed in a two-electrode coin cell (CR2032, MTI). 30 wt% aqueous KOH solution was used as the electrolyte. The electrochemical properties of the supercapacitor electrodes were studied by cyclic voltammetry (CV), galvanostatic charge/discharge (CD) and electrochemical impedance spectroscopy (EIS). All the electrochemical measurements were carried out at room temperature using a CHI electrochemical workstation (Model 660D, CH Instruments).

RESULTS AND DISCUSSION

Figure 1 (a-d) shows FESEM images of the two distinct cobalt sulfide morphologies directly grown over carbon fabric. In both cases, the carbon fiber is uniformly covered with the cobalt sulfide structures. Figure 1(a) and (b) show that the nanoflakes electrode has an average flake thickness of less than 80 nm). In comparison, Figure 1(c) and (d) shows the FESEM images of cobalt sulfide octahedra , which have a rough surface and a fairly large size (1-2 μm), when compared to 2D nanofalkes. Detailed microstructural analysis of the octaheda samples by TEM technique revealed that these structures are composed of several cobalt sulfide nanosheets, as will be discussed shortly.

PXRD pattern of the nanoflake and octahedra samples are shown in Figure 2(a). All diffraction peaks for both samples can be readily indexed to face-centered cubic Co_9S_8 (JCPDS card No. 003-0631) with a space group of Fm-3m. The broad diffraction peaks of nanoflake sample indicate the small size of the Co_9S_8 sample. In the crystal structure of Co_9S_8, S atoms are arranged through cubic closepacking, 8/9 Co atoms are surrounded by a tetrahedron of S atoms, and the rest 1/9 Co atoms are surrounded by an octahedron of S atoms. The nitrogen adsorption isotherms of the Co_9S_8 samples are shown in Figure 2(b), using which the BET surface area values are calculated as 26.80 m^2/g and 10.67 m^2/g respectively for the nanoflake and octahedra samples. The N_2 adsorption isotherms demonstrate that both nanopores and mesopores are present in the samples. The linear increase of N_2 uptake at low pressure range, which is $P/P0 = 0.00–0.1$, indicates a monolayer gas adsorption inside the pores. The adsorption curves show a near plateau region at $P/P0 = 0.2–0.8$, indicating the presence of nanopores together with some mesopores. The sharp increase in the N_2 adsorption curve at $P/P0 = 0.8–1.0$ corresponds to adsorption in the inter-layer/octahedra voids[26]. BET surface area values obtained for the Co_9S_8 nanoflakes in the present study are higher than the values reported in the nice works by Justin and Rangarao (20 m^2/g) [15] and Yan *et al*. (0.3 m^2/g) [27], which is favorable for improved supercapacitor performance. Adsorption average pore width (4V/A by BET) for the Co_9S_8 nanoflake and Co_9S_8 octahedra samples are respectively 7.7830 and 7.1803 nm. The pore size distributions of the samples calculated from adsorption isotherms using Barret-Joyner-Halenda

(BJH) method are shown as inset of Figure 2(b). BJH Adsorption cumulative volume of pores between 1.7000 nm and 300.0000 nm diameter for the nanoflake and octahedra samples are 0.02310 cm^3/g and 0.02132 cm^3/g respectively.

To investigate the microstructure of Co_9S_8 nanostructures in detail, extensive TEM analysis was carried out. TEM and HRTEM images of nanoflake sample are shown in Figure 3 (a and b) which clearly indicates the flexible sheet-like structure. A close inspection of a typical nanosheet reveals that it is highly crystalline in nature. Selected area electron diffraction (SAED) performed on the region shown in Figure 3(b) is shown in Figure 3(c). The SAED pattern indicates the polycrystalline structure of the sample. TEM and HRTEM images and SAED pattern of the octahedral sample are shown in Figure 3(d,e and f). From these micrographs, it is clear that the ultrasonication results in the breakdown of Co_9S_8 octahedra into nanosheets (Figure 3(b)). In fact, the octahedra microstructure is composed of several nanosheets and the nanosheets are composed of crystalline nanoparticles. SAED pattern of the octahedral sample clearly indicates that these nanostructures are having polycrystalline nature. For both the samples, diffraction rings in the SAED pattern can be indexed to the FCC cubic Co_9S_8 crystal structure using circular hough diffraction analysis [28] and these results agree well with the PXRD results.

Since the Co_9S_8 samples were prepared by the sulfuration of Co_3O_4 samples, it is important to ensure the absence of oxygen in the final product. We have therefore employed energy-dispersive spectrometer (EDS) elemental mapping to study the spatial distribution and depth profile of the elements Co, S, and O in both nanoflake and octahedra samples. Figure 4 (a and b) shows the results obtained for Co_9S_8 nanoflakes and Co_9S_8 octahedra samples, respectively. From the elemental mapping of O showing the spatial distribution of oxygen in nanosheet and octahedral samples (Figure 4 [a (iii) and b (iii)]), it is clear that no oxygen is present within the samples, which is further confirmed from the depth profile analysis where the signal intensity of oxygen drops within the sample. These results clearly indicate that both the samples consist of uniformly distributed Co and S without any O. This further ensures that Co_3O_4 nanostructures were completely converted to Co_9S_8 nanostructures. From these results, the mechanism of formation of Co_9S_8 nanostructures can be explained as following. When carbon fabric with the Co_3O_4 nanostructures are immersed in the Na_2S solution, $-S^{2-}$, HS^-, and H_2S in Na_2S solution react with Co_3O_4 and ion-exchange reaction occurs slowly to convert all of the Co_3O_4 to Co_9S_8 homogeneously keeping the original morphology. As the concentration of sulfide ions on the surface of octahedra sample is higher than that inside, cobalt ions on the surface react with sulfide ions in situ violently, leading to the formation of some nanoparticles on the surface [25].

As the Co_9S_8 nanostructures in sheet and octahedra morphologies are both composed of nanosheets formed of numerous nanocrystals, the transportation of aqueous electrolytes through their nanochannels is possibly more feasible for efficient redox reactions during Faradaic charge storage process. However, the charge storage efficiency of the samples can vary due to the observed differences in morphologies leading to a big difference in BET surface area values. In order to identify which morphology is favorable for high-rate capacitive energy storage, the electrochemical-specific material characteristics of these individual electrodes were measured in three-electrode configuration. CV curves for Co_9S_8 samples with nanoflake and octahedra morphologies, measured in a potential window of -0.3 to 0.6 V (vs. Ag/AgCl) at different scan rates, are shown in Figure 5 (a) and (b). At lower scan rates, CV loops for both samples show a distinct pair of redox peaks during the anodic and cathodic sweeps. The shape of the CV curves agrees well with previous reports on Co_9S_8 in KOH solution [25]. The possible electrochemical reactions involved can be described as follows:

$$\mathrm{Co_9S_8} + OH^- \Leftrightarrow Co_9S_8OH + H_2O + e^- \qquad (4)$$

$$Co_9S_8OH + OH^- \Leftrightarrow Co_9S_8O + H_2O + e^- \qquad (5)$$

The gravimetric specific capacitances of the Co_9S_8 nanoflake electrode are 1056, 792, 636 and 455 F/g at scan rates 5, 10, 20 and 50 mV/s. The area of the electrode and mass loading of active materials were 0.5 cm^2 and 1 mg respectively. These values are much higher than those previously reported for Co_9S_8 nanorods in the excellent work on Co_9S_8 Nanorod// Co_3O_4@RuO_2 nanosheet arrays based flexible asymmetric Supercapacitors by Xu et al. (783.3 F/g at 5 mV/s)[25]. In contrast, the octahedra sample exhibited lower specific capacitance values of 88, 58, 41 and 24 F/g at scan rates 5, 10, 20 and 50 mV/s which can be attributed to both the very high mass loading of active material (17 mg) in the sample due to the agglomeration of nanosheets and lower surface area leading to less electrolyte accessibility. The area of the electrode was 1 cm^2. CV curves for Activated carbon sample measured within a potential window of -1 to 0 V (vs. Ag/AgCl) at different scanrates in three electrode configuration are shown in Figure 5 (c). The mass loading of activated carbon was 10 mg. The sample exhibited mainly electric double layer capacitive behavior with specific capacitance values of 123, 102, 81 and 60 F/g at scan rates 5, 10, 20 and 50 mV/s.

Comparison of CV loops of positive and negative electrodes, in 3 electrode configuration, were performed to evaluate the possible electrochemical potential windows of Co_9S_8 nanoflakes//AC and Co_9S_8 octahedra//AC asymmetric hybrid supercapacitors in 30 wt% KOH aqueous electrolyte. Given that the Co_9S_8 and AC electrodes possess stable voltage windows between -0.3 and 0.6 V and between -1 and 0 V, respectively, with regard to the Ag/AgCl reference, it is expected that Co_9S_8//AC asymmetric hybrid supercapacitor test cell could theoretically achieve a maximum working voltage of 1.6 V. In order to obtain a stable asymmetric hybrid supercapacitor operating in a 1.6 V potential window, it is necessary to balance the charges (Q) that stored at both electrodes based on the relationship $Q_- = Q_+$ [7, 29, 30]. The stored charges are proportional to the specific capacitance (C), the potential window (V) and the mass (m) of the electrode, i.e., $Q = CVm$. In other words, $\frac{m_-}{m_+} = \frac{C_+V_+}{C_-V_-}$. The optimum mass ratios of AC and Co_9S_8 nanostructures have been calculated and Co_9S_8 nanosheets// AC and Co_9S_8 octahedra//AC asymmetric hybrid supercapacitor test cells are fabricated. CV curves of optimized Co_9S_8 nanosheets// AC and Co_9S_8 octahedra//AC asymmetric hybrid supercapacitors at different potential windows at a scan rate of 50mV/s are shown in Figure 6 (a) and (b) respectively, which confirm that these devices can be safely operated in a potentential window of 0 to 1.6 V.

Electrochemical performance of the fabricated asymmetric hybrid supercapacitor test cells are evaluated in two electrode configuration. Figure 7 (a) and (c) respectively shows the CV curves of the Co_9S_8 nanoflake//AC and Co_9S_8 octahedra//AC asymmetric hybrid supercapacitors at various scan rates. As expected, the CV curves of these asymmetric hybrid supercapacitors demonstrate that the stable potential window is extended to 1.6 V. The shapes of CV curves of the capacitors do not change,with the increase of scan rate from 5 to 100 mV/s, implying their excellent electrochemical performance. At the same time, no oxygen or hydrogen evolution current is observed in these curves, indicating that no hydrogen or oxygen evolution occurs within the voltage range (1.6 V). From these CV curves it can also be observed that the redox reactions have occurred. In order to further evaluate the performance of these asymmetric hybrid supercapacitor cells, galvanostatic charge/discharge measurements are conducted at various current densities, and the results for Co_9S_8 nanosheets//AC and Co_9S_8 octahedra//AC asymmetric hybrid supercapacitors are shown in Figure 8(b) and (d) respectively. The galvanostatic charge/discharge curves are not in triangular shape, which may be due to the pseudocapacitance arising out from the redox reaction within this voltage range. From the slope of the discharge curve, capacitance (C) and the gravimetric cell capacitance C_g of each asymmetric device in two electrode configuration are calculated using the formulae,

$$C = \frac{I}{\left(\Delta V / \Delta t\right)} \quad \text{and} \quad C_g = \frac{C}{M} \qquad (6)$$

where 'I' is the constant current for charge- discharge, $\Delta V / \Delta t$ is slope of the discharge curve. 'M' is the total mass of active materials in both electrodes. A C_g of 83 F/g is achieved for Co_9S_8 nanosheets//AC asymmetric hybrid supercapacitor (M= 8 mg) at a constant current density of 1.25 A/g. Whereas, Co_9S_8 octahedra//AC asymmetric hybrid supercapacitor exhibited only a low value of 18.6 F/g at a constant current density of 1 A/g due the high mass loading (M= 26 mg).

For comparison, symmetric AC//AC capacitor is also assembled and tested. The results obtained from CV measurements and galavanostatic charge discharge measurements in a potential window of 0 to 1V for the symmetric supercapacitor are shown in Fig 7 (e) and (f) respectively. The AC//AC symmetric supercapacitor device retains rectangular CV loops, which are characteristics for supercapacitors with low contact resistance, indicating an excellent capacitance behavior and low contact resistance. From Fig 7(f) it is evident that the charge-discharge curves are nearly linear and symmetrical as in the case of a electric double layer capacitor capacitor. Voltage (IR) drop is observed to be very small, which indicates that the electrodes have low internal resistance. A C_g of 44.8 F/g is achieved for AC//AC symmetric supercapacitor (M= 8 mg) at a constant current density of 1.25 A/g.

Variations in gravimetric cell capacitance of Co_9S_8 nanoflakes//AC and Co_9S_8 octahedra//AC asymmetric hybrid supercapacitors and AC//AC symmetric supercapacitors with increase in current density are shown in Figure 8(a). In all cases the capacitance decreases when the current density increases. At lower current densities, ions can penetrate into the inner-structure of electrode material, having access to almost all available pores of the electrode, but at higher current densities, an effective utilization of the material is limited only to the outer surface of electrodes. It results in the reduction of specific capacitance values. From the graph, it is clear that the gravimetric cell capacitance of the Co_9S_8 nanoflakes//AC asymmetric hybrid supercapacitor is much higher than that of the AC//AC symmetric capacitor at the same current density. Rate performance of a supercapacitor is determined from its capacity retention ratio as a function of the current density. Rate capacities of 84, and 58 % respectively are obtained for Co_9S_8 nanoflakes//AC and Co_9S_8 octahedra//AC asymmetric hybrid supercapacitors. The superior electrochemical capacitive performance of the Co_9S_8 nanoflakes//AC asymmetric hybrid supercapacitor can be attributed to the combined contribution of redox pseudocapacitance and 2D morphology of Co_9S_8 nanoflakes and the electric double layer capacitance of AC. The cycling stabilities of the asymmetric and symmetric supercapacitors upon continuous galvanostatic charge/discharge cycling at a constant current density of 3 A/g is illustrated in Figure 8(b). After 5000 cycles, AC//AC symmetric capacitor retains 90% of its initial capacitance. % retention of gravimetric cell capacitance of Co_9S_8 nanoflakes//AC and Co_9S_8 octahedra//AC asymmetric hybrid supercapacitors are 89.5 and 65 respectively. Matching of cycling stability of Co_9S_8 nanoflakes//AC asymmetric hybrid supercapacitor with that of AC//AC symmetric capacitor demonstrates the excellent electrochemical stability of the former during the cycling test. The Ragone plot relative to the corresponding energy and power densities for the Co_9S_8 nanoflakes//AC and Co_9S_8 octahedra//AC asymmetric hybrid supercapacitors and AC//AC symmetric capacitor are shown in Figure 8(c). The energy and power data are calculated by taking account of total mass of material in both electrodes. Ragone plot of Co_9S_8 octahedra//AC asymmetric hybrid supercapacitor is comparable to that of AC//AC symmetric capacitor. The Co_9S_8 nanoflakes//AC asymmetric hybrid supercapacitor shows a much higher energy density than the symmetric capacitor and at the same time it keeps a very good power density. The energy density of Co_9S_8 nanoflakes//AC asymmetric hybrid supercapacitor increases from 26.3Wh/kg to 31.4 Wh/kg when the power density decreases from 4000 W/kg to 200W/kg. The specific energy increases by more than three times compared with that of a symmetric AC//AC symmetric capacitor. The fabricated Co_9S_8 nanoflakes//AC asymmetric hybrid supercapacitor exhibits a much improved energy density at high power density in comparison with Co_3O_4//AC asymmetric hybrid supercapacitor (24.9 Wh/kg at 0.225 kW/kg) [6], $Co(OH)_2$-nanowires//AC asymmetric supercapacitor (13.6 Wh/kg at 0.153 kW/kg) [31], Ni–Co oxide//AC asymmetric device (7.4 Wh/kg at 1.90 kW/kg) [32], and (Ni_3S_2/Carbon Nanotube Composites)//AC asymmetric supercapacitor(19.8 Wh/kg at 0.798 kW/kg) [33] .

The superior capacitive performance of Co_9S_8 nanosheets//AC asymmetric hybrid supercapacitor in comparison with that of Co_9S_8 octahedra //AC asymmetric hybrid supercapacitor can be attributed to the 2D morphology of the Co_9S_8 nanoflakes grown directly over conducting carbon cloth. The 2D morphology provides more electrolyte accessible electroactive surface area, as confirmed from the BET analysis. Due to direct growth on carbon cloth, each nanoflake has its own electric contact with the conducting substrate ensuring the participation of all nanoflakes in electrochemical reaction. Furthermore, Co_9S_8 nanoflakes electrode is having lower internal resistance as the open space between neighboring flakes/sheets facilitates the diffusion of KOH electrolyte into the inner region of the electrode. In Co_9S_8 octahedra, nanosheets are organized into very large octahedra particles (1-2 μm), reducing the electrolyte accessible electroactive surface area and hence, the pseudocapacitive performance.

A deep insight into the resistive and capacitive behaviors of asymmetric cells can be obtained from EIS analysis performed in the frequency range from 100 k Hz to 10 m Hz at open circuit voltage by applying a 5 mV signal. The resulting Nyquist plots for Co_9S_8 nanosheets//AC asymmetric hybrid supercapacitor is shown in Figure 9(a). The plot is composed of a semicircle in the high-frequency region and a straight line making an angle 45° with the real axis in the low-frequency region. This line is called Warburg line which is a result of the frequency dependence of ion diffusion in the electrolyte to the electrode interface. The real axis intercept at high frequency corresponds to the uncompensated resistance of the bulk electrolyte solution (R_s) and it is also known as equivalent series resistance (ESR). The diameter of semicircle in the high frequency range gives the value of charge transfer resistance (R_{ct}). R_{ct} depends on electrolyte accessible area and electrical conductivity of the electrode material. The larger the electroactive surface area, the lower the charge-transfer resistance. ESR and R_{ct} values for Co_9S_8 nanosheets//AC asymmetric hybrid supercapacitor are 1.18 and 0.7 Ω respectively. These lower values indicate consistent interfacial contact between the Co_9S_8 nanoflakes and the carbon fibers. EIS spectra for Co_9S_8 octahedra//AC asymmetric hybrid supercapacitor is shown in Fig 9(b). The plot shows two partial semicircles at high and medium frequency regions which can be attributed to the different charge propagation phenomena in the system as a result of Faradaic reactions. A simple equivalent circuit model to evaluate this kind of EIS spectra is shown in Figure 9(c**)**. The enlarged view of the semicircle at higher frequency region is shown as the inset of Figure 9(b), which is characteristic of the processes occurring at the oxide–electrolyte interface and can be modeled as a double layer capacitor $C_{D.L}$ in parallel with a charge transfer resistor (R_{ct}) in the equivalent circuit. R_{ct} can be measured directly as the semicircle diameter and is due to some discontinuity in the charge transfer process at the electrode/electrolyte interface. The second partial kinetic semicircle at medium frequency region corresponds to the charge-transfer resistance due to Faradaic redox processes in the system which involves the exchange of OH^- ions. This impedance characteristic can be modeled as a film impedance due to the Faradaic redox processes involving electron hopping in the Co_9S_8 surface layer and OH^- ion diffusion, which is assumed to be consisting of a film capacitor, C_f, in parallel with an electron-transfer resistor, R_e. At a lower frequency region Nyquist plot is nearly vertical linear, which corresponds to the Pseudocapacitance $C_{p.}$ ESR and R_{ct} and R_e values for Co_9S_8 nanooctahedra//AC asymmetric hybrid supercapacitor are 1.58, 0.7 and 18 Ω respectively. The electron charge transfer resistance in the medium frequency region is large for the octahedra sample. This indicates that it should have lower surface area than the nanoflake sample. This agrees well with the BET results. ESR data is an important factor in determining the maximum possible power density of a supercapacitor. The maximum power density (P_{max}) of the supercapacitor devices are calculated from the low frequency data of the impedance spectra, according to the equation (7).

$$P_{\max} = \frac{V_i^2}{4MR} \qquad (7)$$

where V_i is the initial voltage (here it is 1.6 V), R is the ESR and M is the total mass of the two electrodes. Maximum power densities of 67.8 and 15.6 kW/kg are obtained respectively for Co_9S_8 nanosheets//AC and Co_9S_8 octahedra//AC asymmetric hybrid supercapacitors. These results demonstrate that the Co_9S_8 nanoflakes//AC asymmetric hybrid supercapacitor is a very promising electrochemical capacitor with both high energy and power densities.

CONCLUSIONS

We report the synthesis of cobalt sulfide-on-fiber nanostructures as electrodes for asymmetric hybrid supercapacitors. The 2D Co_9S_8 electrodes show superior electrochemical properties and are used in the fabrication of asymmetric hybrid supercapacitors. The hybrid capacitors use 2D Co_9S_8 as positive electrode and AC as negative electrodes in KOH aqueous electrolyte. The optimized 2D Co_9S_8 nanoflakes//AC asymmetric hybrid supercapacitors can be operated reversibly in a wide potential window as high as 1.6 V and deliver a high energy density of 31.4 Wh/kg, which is much higher than many of metal oxide//AC asymmetric hybrid supercapacitors. Furthermore, the Co_9S_8 nanoflakes//AC asymmetric hybrid supercapacitor exhibits long-term cycling stability with 90% capacitance retention after 5000 cycles. These results offer a convenient and efficient way to fabricate asymmetric hybrid supercapacitors based on 2D electrode materials for efficient energy storage applications.

ACKNOWLEDGEMENTS

Research reported in this publication has been supported by King Sbdullah University of Science & Technology (KAUST). Authors thank the ‘Advanced nanofabricationNanofabrication, Imaging and Characterization Laboratory ’and ‘Analytical Chemistry Laboratory’ at KAUST. R.B.R. acknowledges the financial support from SABIC Post- Doctoral Fellowship.

REFERENCES

1. M. Conte, *Fuel Cells*, 2010, **10**, 806-818.
2. G. P. Wang, L. Zhang and J. J. Zhang, *Chemical Society Reviews*, 2012, **41**, 797-828.
3. E. G. Calvo, A. Arenillas, J. A. Menendez, M. Gonzalez and J. C. Viera, *Afinidad*, 2009, **66**, 380-387.
4. P. Simon and Y. Gogotsi, *Nature Materials*, 2008, **7**, 845-854.
5. J. G. Wang, Y. Yang, Z. H. Huang and F. Y. Kang, *Carbon*, 2013, **61**, 190-199.
6. C. M. Zhang, L. J. Xie, W. Song, J. L. Wang, G. H. Sun and K. X. Li, *Journal of Electroanalytical Chemistry*, 2013, **706**, 1-6.
7. J. C. Huang, P. P. Xu, D. X. Cao, X. B. Zhou, S. N. Yang, Y. J. Li and G. L. Wang, *Journal of Power Sources*, 2014, **246**, 371-376.
8. X. Wang, C. Y. Yan, A. Sumboja and P. S. Lee, *Nano Energy*, 2014, **3**, 119-126.
9. K. Naoi, W. Naoi, S. Aoyagi, J. Miyamoto and T. Kamino, *Accounts of Chemical Research*, 2013, **46**, 1075-1083.
10. F. X. Wang, S. Y. Xiao, Y. Y. Hou, C. L. Hu, L. L. Liu and Y. P. Wu, *Rsc Advances*, 2013, **3**, 13059-13084.
11. L. J. Xie, J. F. Wu, C. M. Chen, C. M. Zhang, L. Wan, J. L. Wang, Q. Q. Kong, C. X. Lv, K. X. Li and G. H. Sun, *Journal of Power Sources*, 2013, **242**, 148-156.
12. H. Z. Wan, X. Ji, J. J. Jiang, J. W. Yu, L. Miao, L. Zhang, S. W. Bie, H. C. Chen and Y. J. Ruan, *Journal of Power Sources*, 2013, **243**, 396-402.
13. J. W. Xiao, L. Wan, S. H. Yang, F. Xiao and S. Wang, *Nano Letters*, 2014, **14**, 831-838.
14. F. Tao, Y. Q. Zhao, G. Q. Zhang and H. L. Li, *Electrochemistry Communications*, 2007, **9**, 1282-1287.
15. P. Justin and G. R. Rao, *International Journal of Hydrogen Energy*, 2010, **35**, 9709-9715.
16. M. Jayalakshmi and M. M. Rao, *Journal of Power Sources*, 2006, **157**, 624-629.
17. C. J. Raj, B. C. Kim, W. J. Cho, W. G. Lee, Y. Seo and K. H. Yu, *Journal of Alloys and Compounds*, 2014, **586**, 191-196.
18. J. M. Soon and K. P. Loh, *Electrochemical and Solid State Letters*, 2007, **10**, A250-A254.
19. S. W. Chou and J. Y. Lin, *Journal of the Electrochemical Society*, 2013, **160**, D178-D182.
20. J. Pu, Z. H. Wang, K. L. Wu, N. Yu and E. H. Sheng, *Physical Chemistry Chemical Physics*, 2014, **16**, 785-791.
21. S. J. Bao, C. M. Li, C. X. Guo and Y. Qiao, *Journal of Power Sources*, 2008, **180**, 676-681.
22. J. Y. Lin and S. W. Chou, *Rsc Advances*, 2013, **3**, 2043-2048.
23. Q. Chen, H. X. Li, C. Y. Cai, S. Yang, K. Huang, X. L. Weiab and J. X. Zhong, *Rsc Advances*, 2013, **3**, 22922-22926.
24. W. Xing, S. Z. Qiao, X. Z. Wu, X. L. Gao, J. Zhou, S. P. Zhuo, S. B. Hartono and D. Hulicova-Jurcakova, *Journal of Power Sources*, 2011, **196**, 4123-4127.
25. J. Xu, Q. F. Wang, X. W. Wang, Q. Y. Xiang, B. Hang, D. Chen and G. Z. Shen, *Acs Nano*, 2013, **7**, 5453-5462.
26. Z.-C. Yang, C.-H. Tang, Y. Zhang, H. Gong, X. Li and J. Wang, *Scientific Reports*, 2013, **3**.
27. J. M. Yan, H. Z. Huang, J. Zhang, Z. J. Liu and Y. Yang, *Journal of Power Sources*, 2005, **146**, 264-269.
28. D. R. G. Mitchell, *Ultramicroscopy*, 2008, **108**, 367-374.
29. P. Y. Tang, Y. Q. Zhao, C. L. Xu and K. P. Ni, *Journal of Solid State Electrochemistry*, 2013, **17**, 1701-1710.

30. S. Vaquero, J. Palma, M. Anderson and R. Marcilla, *International Journal of Electrochemical Science*, 2013, **8**, 10293-10307.
31. Y. Tang, Y. Liu, S. Yu, S. Mu, S. Xiao, Y. Zhao and F. Gao, *Journal of Power Sources*, 2014, **256**, 160-169.
32. C. Tang, Z. Tang and H. Gong, *Journal of the Electrochemical Society*, 2012, **159**, A651-A656.
33. C.-S. Dai, P.-Y. Chien, J.-Y. Lin, S.-W. Chou, W.-K. Wu, P.-H. Li, K.-Y. Wu and T.-W. Lin, *Acs Applied Materials & Interfaces*, 2013, **5**, 12168-12174.

FIGURE CAPTIONS

1. (a) Low and (b) high magnification SEM images of Co_9S_8 nanoflakes. (c) Low and (d) high magnification SEM images of Co_9S_8 octahedra.
2. (a) Powder X-ray diffraction pattern and (b) nitrogen adsorption isotherms of Co_9S_8 nanostructures. Inset of (b) pore size distributions of Co_9S_8 nanostructures.
3. (a) Low and (b) High magnification TEM images and (c) Selected area electron diffraction pattern of Co_9S_8 nanoflakes. (d) Low and (e) High magnification TEM images and (f) Selected area electron diffraction pattern of Co_9S_8 octahedra.
4. (a) EDS elemental mapping of (i) Co,(ii)S and (iii) O and (iv) corresponding depth profile analysis for Co_9S_8 nanoflakes. (b) EDS elemental mapping of (i) Co,(ii)S and (iii) O and (iv) corresponding depth profile analysis for Co_9S_8 octahedra.
5. Cyclic voltammograms of (a) Co_9S_8 nanoflakes, (b) Co_9S_8 octahedra and (c) AC at different scanrates in three electrode configuration.
6. Cyclic voltammograms of optimized (a) Co_9S_8 nanosheets// AC and (b) Co_9S_8 octahedra//AC asymmetric hybrid supercapacitors at different potential windows at a scan rate of 50mV/s.
7. Cyclic voltammograms of (a) Co_9S_8 nanoflake//AC and (c) Co_9S_8 octahedra//AC asymmetric hybrid supercapacitors and (e) AC//AC symmetric supercapacitor at different scanrates. Galvanostatic charge- discharge curves of (b) Co_9S_8 nanoflake//AC and (d) Co_9S_8 octahedra//AC asymmetric hybrid supercapacitors and (f) AC//AC symmetric supercapacitor at different current densities.
8. Comparison of (a) gravimetric cell capacitances, (b) Cycling performance, and (c) Ragone plot (power density vs. energy density) of Co_9S_8 nanoflake//AC and Co_9S_8 octahedra//AC asymmetric hybrid supercapacitors and AC//AC symmetric

supercapacitor. The energy and power densities were derived from the charge–discharge curves at different current densities.

9. Nyquist plots for (a) Co_9S_8 nanoflake//AC and (b) Co_9S_8 octahedra//AC asymmetric hybrid supercapacitors and (c) Equivalent circuit model for the impedance spectra of Co_9S_8 octahedra//AC asymmetric hybrid supercapacitor.

FIGURES

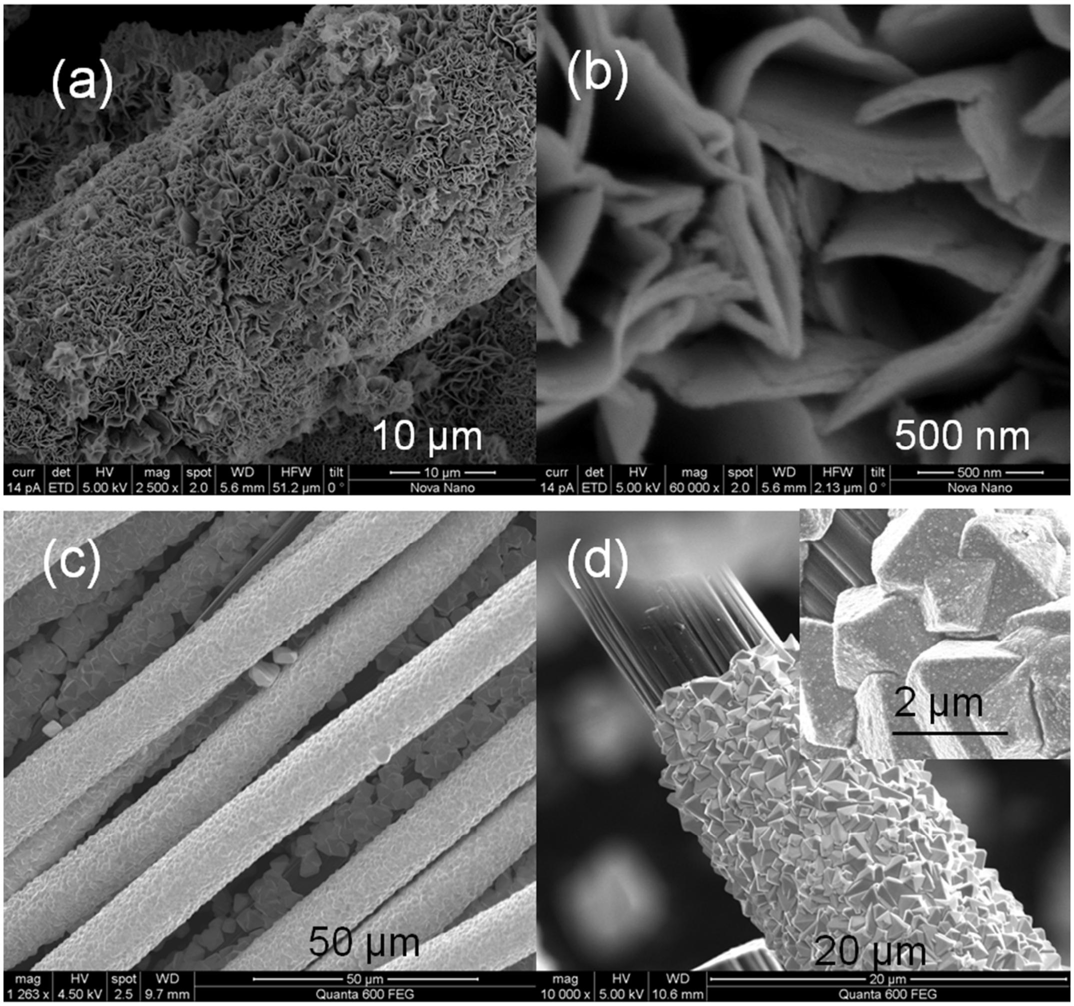

Figure1

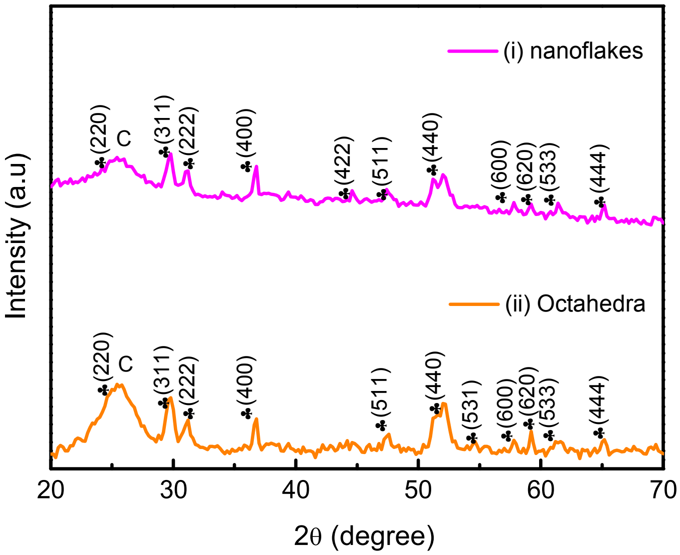

Figure 2(a)

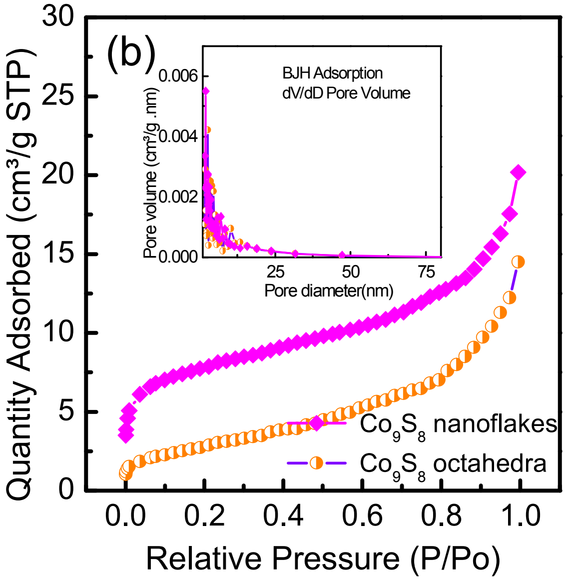

Figure 2(b)

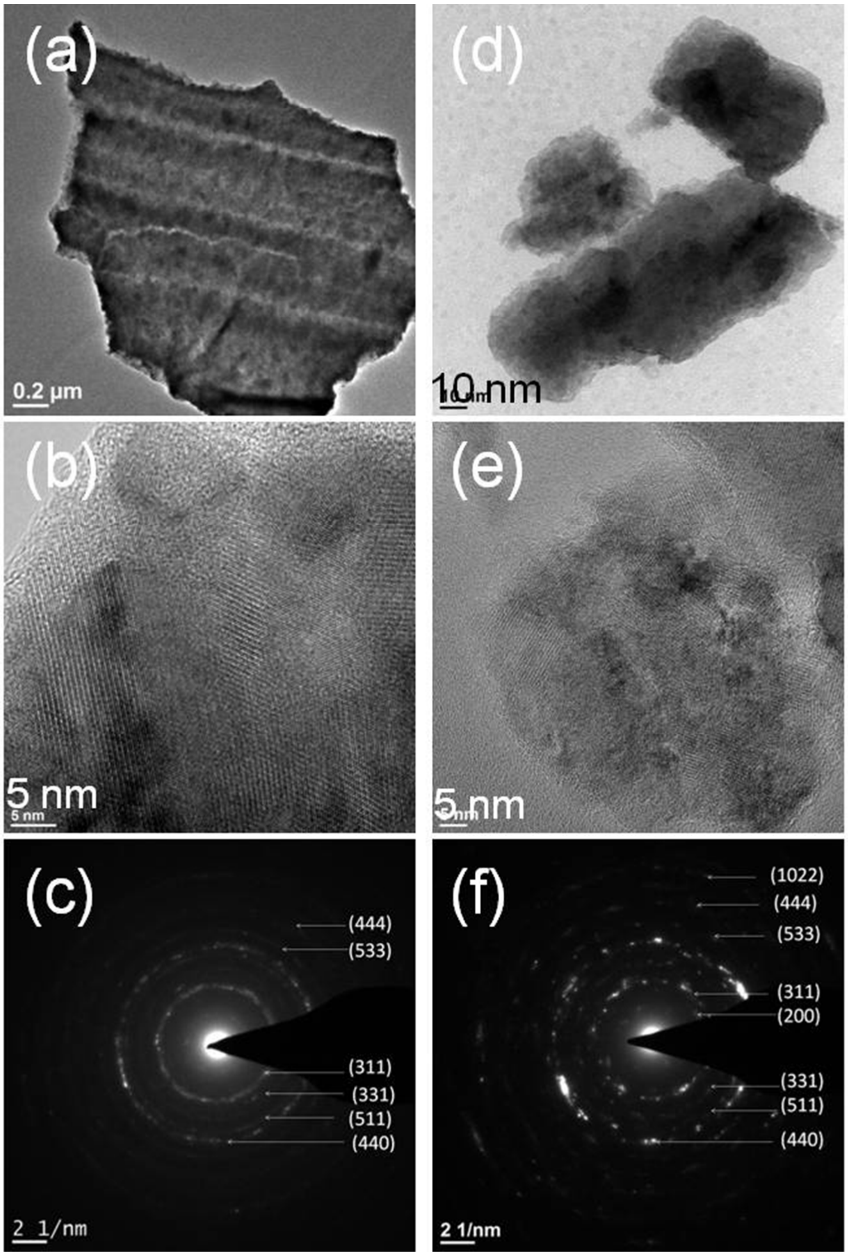
(a)
0.2 µm
(d)
10 nm
(b)
5 nm
(e)
5 nm
(c)
(444)
(533)
(311)
(331)
(511)
(440)
2 1/nm
(f)
(1022)
(444)
(533)
(311)
(200)
(331)
(511)
(440)
2 1/nm

Figure 3

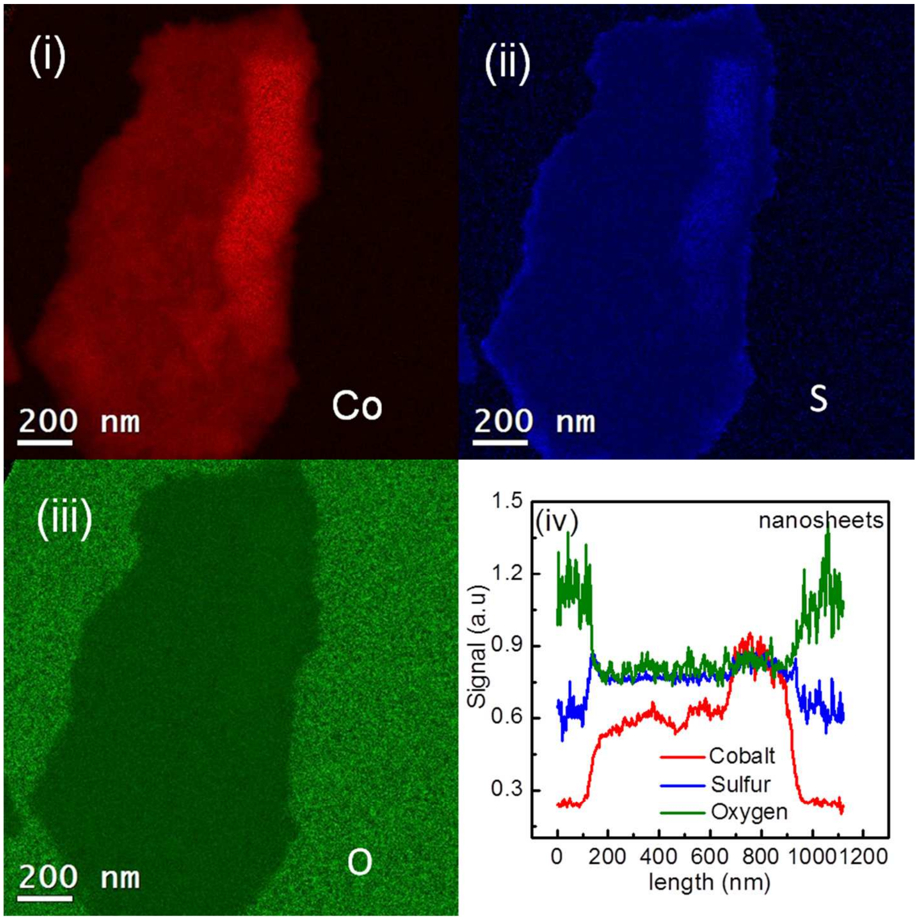
(i)
Co
200 nm
(ii)
S
200 nm
(iii)
O
200 nm
(iv)
nanosheets
Signal (a.u)
1.5
1.2
0.9
0.6
0.3
0
200
400
600
800
1000
1200
length (nm)
Cobalt
Sulfur
Oxygen

Figure 4(a)

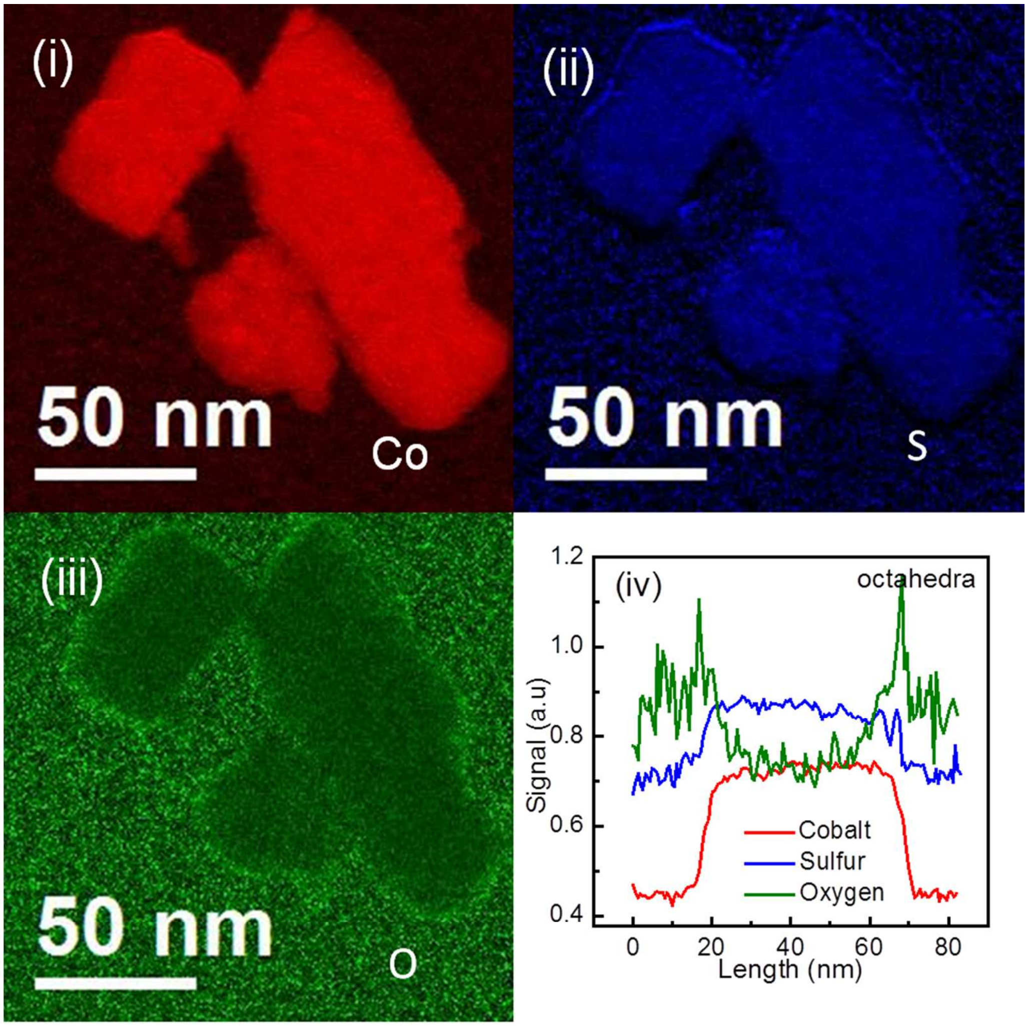
(i)
50 nm
Co
(ii)
50 nm
S
(iii)
50 nm
O
(iv)
octahedra
Signal (a.u)
Length (nm)
1.2
1.0
0.8
0.6
0.4
0
20
40
60
80
Cobalt
Sulfur
Oxygen

Figure 4(b)

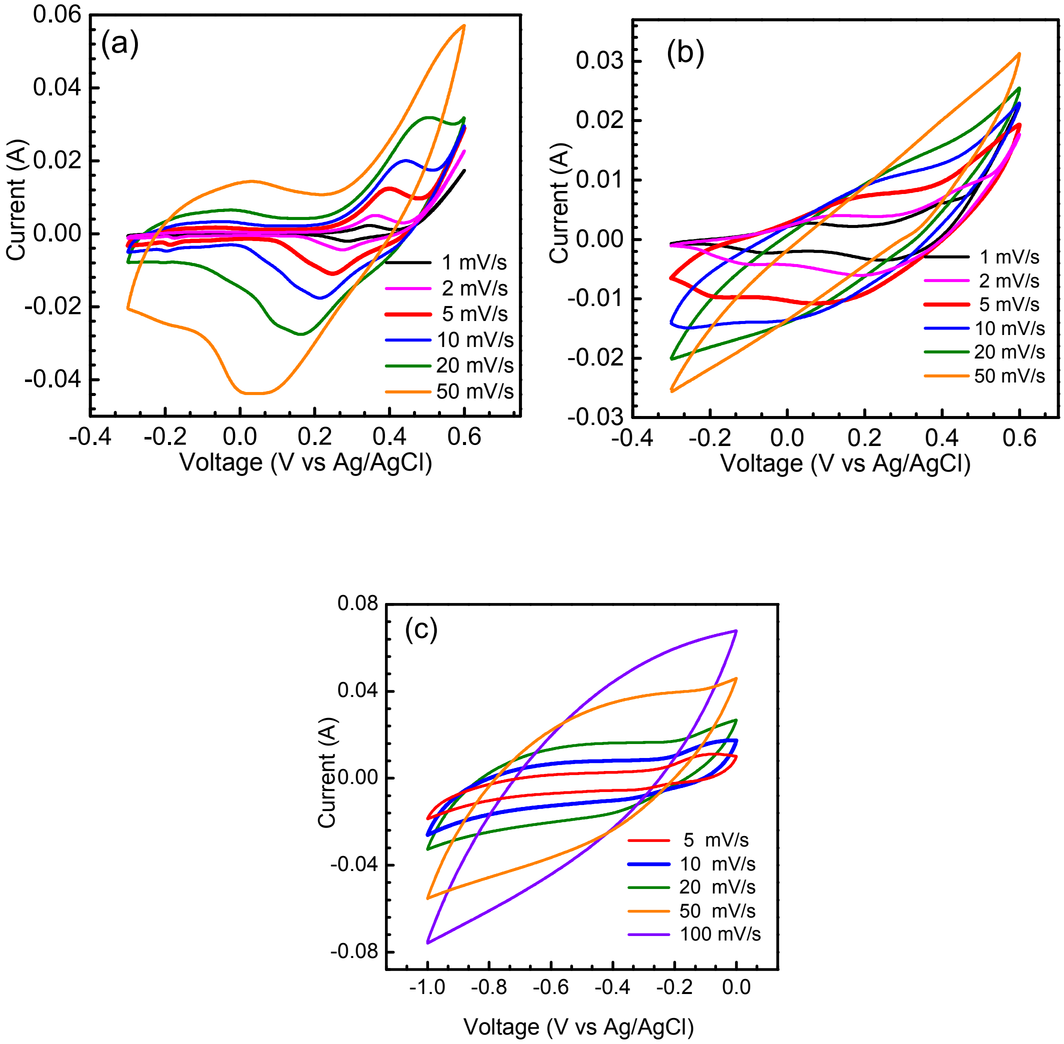
(a)
Current (A)
0.06
0.04
0.02
0.00
-0.02
-0.04
-0.4
-0.2
0.0
0.2
0.4
0.6
Voltage (V vs Ag/AgCl)
1 mV/s
2 mV/s
5 mV/s
10 mV/s
20 mV/s
50 mV/s
(b)
Current (A)
0.03
0.02
0.01
0.00
-0.01
-0.02
-0.03
-0.4
-0.2
0.0
0.2
0.4
0.6
Voltage (V vs Ag/AgCl)
1 mV/s
2 mV/s
5 mV/s
10 mV/s
20 mV/s
50 mV/s
(c)
Current (A)
0.08
0.04
0.00
-0.04
-0.08
-1.0
-0.8
-0.6
-0.4
-0.2
0.0
Voltage (V vs Ag/AgCl)
5 mV/s
10 mV/s
20 mV/s
50 mV/s
100 mV/s

Figure 5

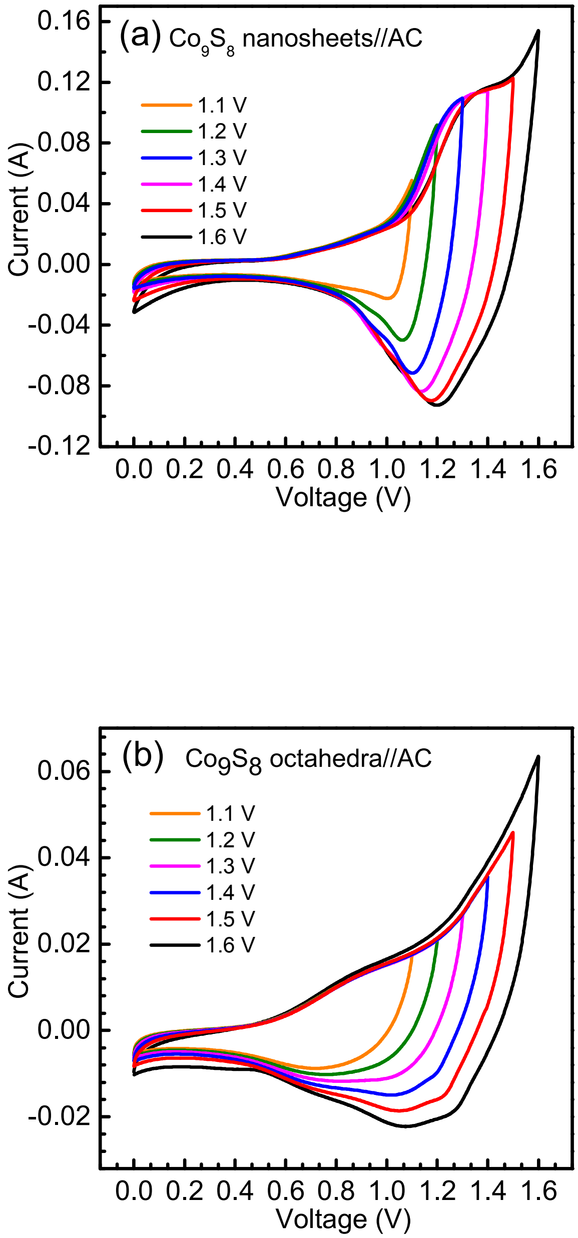
(a) Co_9S_8 nanosheets//AC
1.1 V
1.2 V
1.3 V
1.4 V
1.5 V
1.6 V
Current (A)
0.16
0.12
0.08
0.04
0.00
-0.04
-0.08
-0.12
0.0 0.2 0.4 0.6 0.8 1.0 1.2 1.4 1.6
Voltage (V)
(b) Co_9S_8 octahedra//AC
1.1 V
1.2 V
1.3 V
1.4 V
1.5 V
1.6 V
Current (A)
0.06
0.04
0.02
0.00
-0.02
0.0 0.2 0.4 0.6 0.8 1.0 1.2 1.4 1.6
Voltage (V)

Figure 6

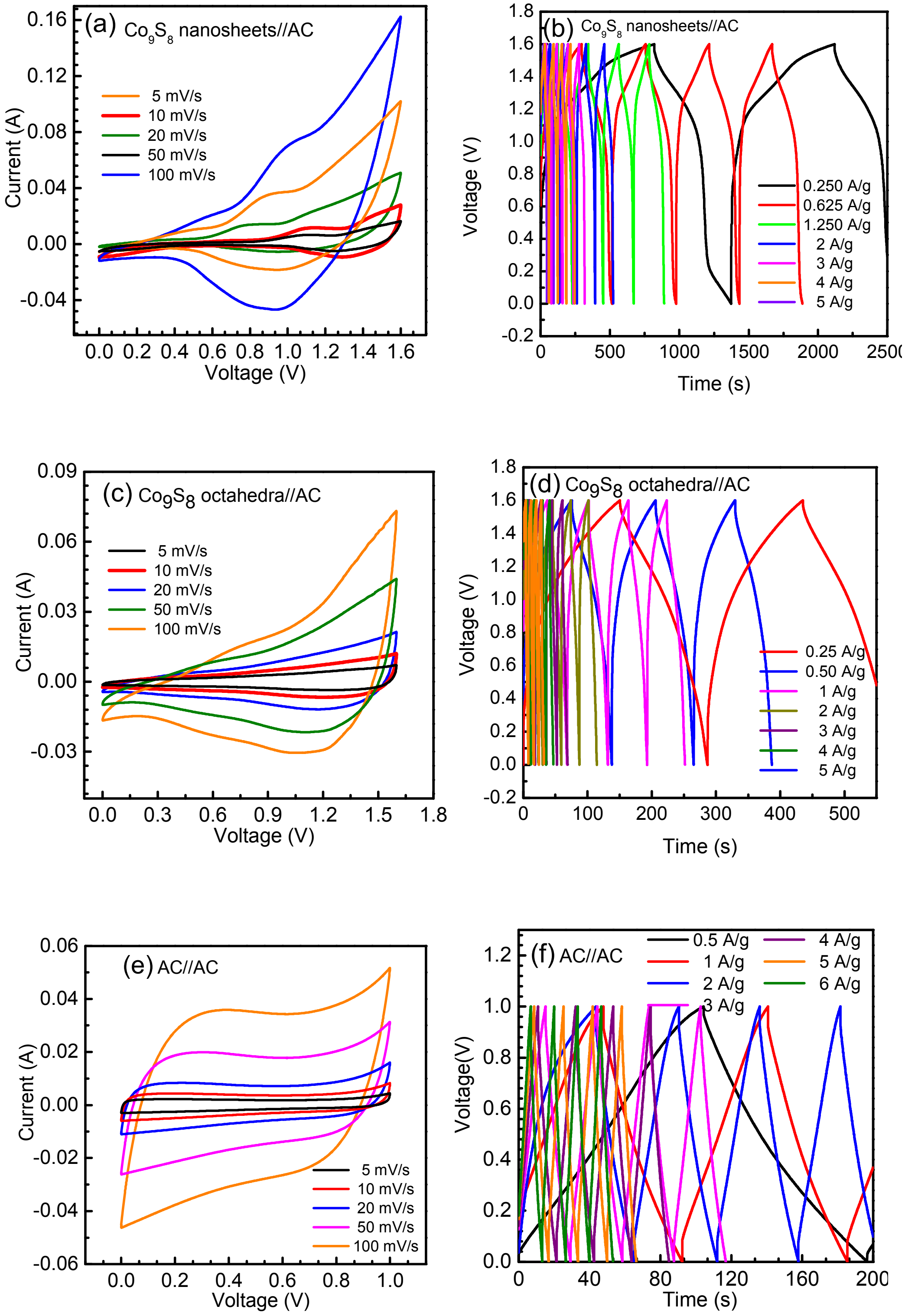
(a) Co9S8 nanosheets//AC
5 mV/s
10 mV/s
20 mV/s
50 mV/s
100 mV/s
Current (A)
Voltage (V)
(b) Co9S8 nanosheets//AC
0.250 A/g
0.625 A/g
1.250 A/g
2 A/g
3 A/g
4 A/g
5 A/g
Voltage (V)
Time (s)
(c) Co9S8 octahedra//AC
5 mV/s
10 mV/s
20 mV/s
50 mV/s
100 mV/s
Current (A)
Voltage (V)
(d) Co9S8 octahedra//AC
0.25 A/g
0.50 A/g
1 A/g
2 A/g
3 A/g
4 A/g
5 A/g
Voltage (V)
Time (s)
(e) AC//AC
5 mV/s
10 mV/s
20 mV/s
50 mV/s
100 mV/s
Current (A)
Voltage (V)
(f) AC//AC
0.5 A/g
1 A/g
2 A/g
3 A/g
4 A/g
5 A/g
6 A/g
Voltage(V)
Time (s)

Figure 7

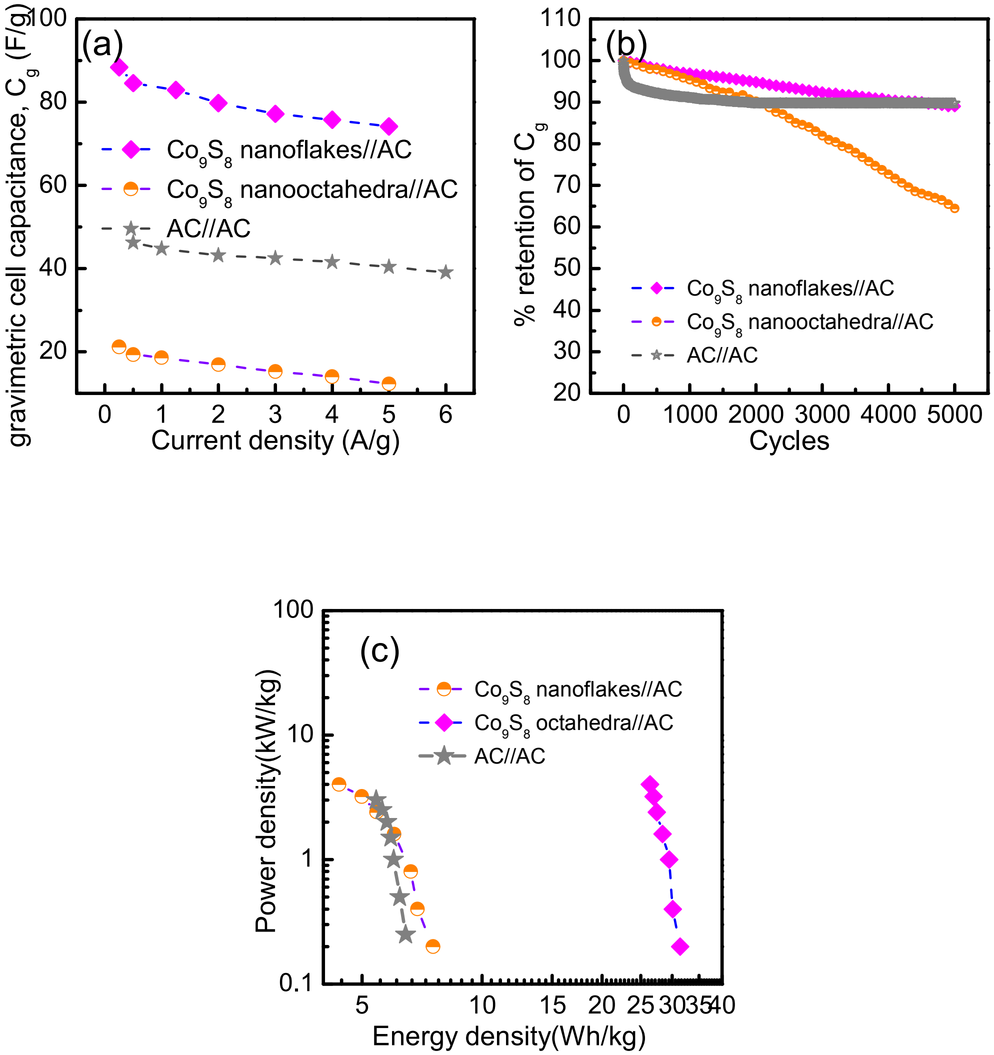
(a)
gravimetric cell capacitance, C_g (F/g)
100
80
60
40
20
0
1
2
3
4
5
6
Current density (A/g)
Co_9S_8 nanoflakes//AC
Co_9S_8 nanooctahedra//AC
AC//AC
(b)
% retention of C_g
110
100
90
80
70
60
50
40
30
20
0
1000
2000
3000
4000
5000
Cycles
Co_9S_8 nanoflakes//AC
Co_9S_8 nanooctahedra//AC
AC//AC
(c)
Power density(kW/kg)
100
10
1
0.1
5
10
15
20
25
30
35
40
Energy density(Wh/kg)
Co_9S_8 nanoflakes//AC
Co_9S_8 octahedra//AC
AC//AC

Figure 8

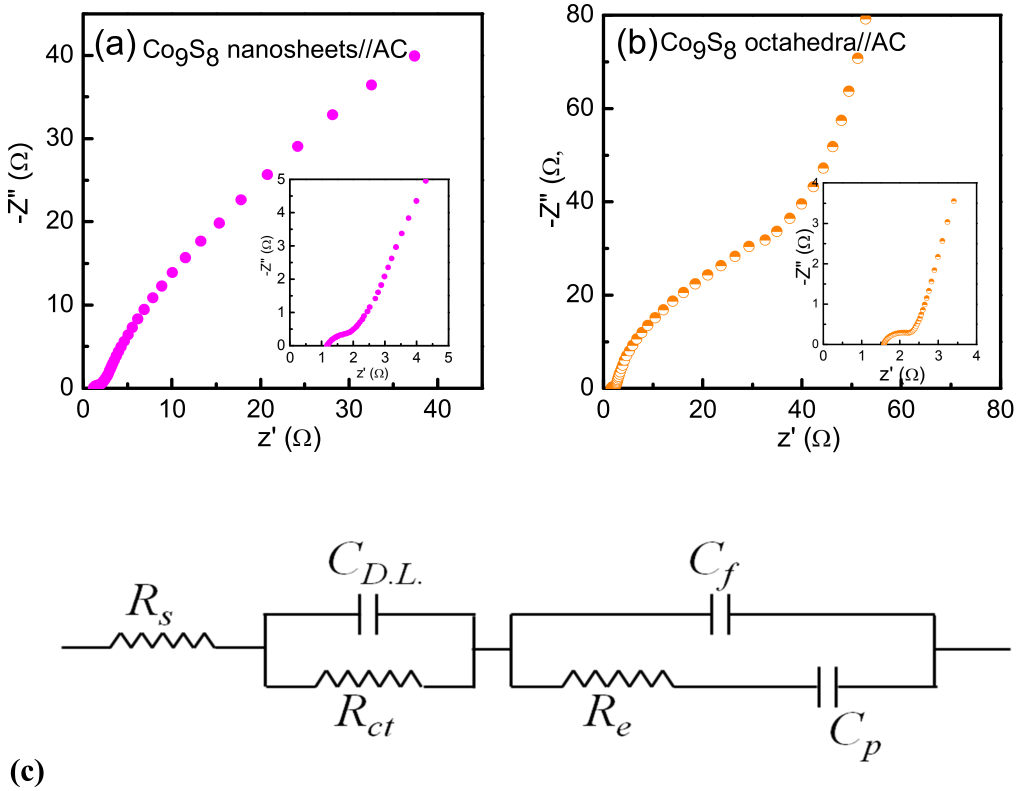
(a) Co9S8 nanosheets//AC
-Z'' (Ω)
z' (Ω)
0
10
20
30
40
(b) Co9S8 octahedra//AC
-Z'' (Ω)
z' (Ω)
0
20
40
60
80
R_s
C_D.L.
R_ct
C_f
R_e
C_p
(c)

Figure 9

Table of Contents Image

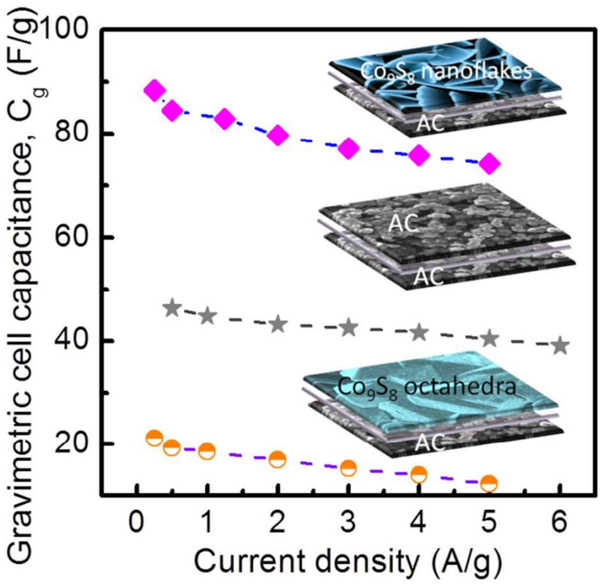

Nanostructured cobalt sulfide-on-fiber with tunable morphology as electrodes for asymmetric hybrid supercapacitors

R.B. Rakhi, Nuha Alhebshi, D.H. Anjum and H.N. Alshareef*

Material Science and Engineering, King Abdullah University of Science and Technology
(KAUST), Thuwal 23955-6900, Saudi Arabia

*Corresponding author: husam.alshareef@kaust.edu.sa

Phone: Office: +966-(0)2-808-4477 | Cell: +966-(0)5-44700037

Table of Contents Image

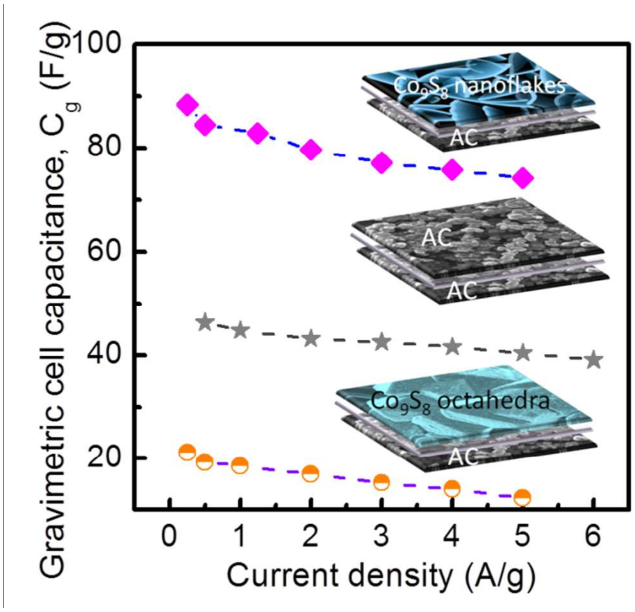

Porous cobalt sulfide (Co_9S_8) nanostructures with tunable morphology directly nucleated over carbon fiber are evaluated as electrodes for asymmetric hybrid supercapacitors.